Chapter 8

END-WALL BOUNDARY LAYER ANALYSIS

The flow in the end-wall regions has a substantial influence on the aerodynamic performance of axial-flow compressors. As noted in Chapter 6, a significant portion of the losses in axial-flow compressors is directly associated with the end-wall flow. The through-flow analysis of Chapter 7 requires some external specification of the viscous end-wall blockage factor for solution of Eq. (7-5). In addition, individual stage loading limits and the compressor surge flow limit are often associated with end-wall stall. Unfortunately, there is no available theoretical aerodynamic model capable of predicting the detailed behavior of these highly complex end-wall flows. Indeed, even modern computational fluid dynamics (CFD) viscous flow solvers are found to be incapable of resolving many of the important flow patterns that are observed in the end-wall regions of axial-flow compressors. When fundamental analysis techniques are not sufficient to treat a problem of interest, engineers commonly resort to a combination of theoretical and empirical models. That approach is always used when formulating an aerodynamic performance analysis for axial-flow compressors. The role of end-wall boundary layer models used within specific performance analyses varies considerably. It is always necessary to address the problem of end-wall blockage effects to effectively apply an inviscid through-flow analysis to the problem. Attempts to model end-wall work and loss effects from boundary layer analysis results will be briefly discussed in this chapter. But, in this writer's experience, none of the available end-wall boundary layer models is sufficiently accurate and reliable for that purpose. Chapter 6 has already described empirical models used to extend cascade loss models to account for clearance and end-wall loss effects.

This chapter presents an end-wall boundary layer analysis used to account for end-wall boundary layer blockage effects. The blade row performance models of Chapter 6, the through-flow analysis of Chapter 7 and this end-wall boundary layer analysis are the basic components of an aerodynamic performance analysis. Chapter 9 describes the performance analysis and qualifies it by comparing performance predictions with experimental data. In keeping with the stated objective of this book, Chapters 6 through 9 provide a detailed description of the aerodynamic performance analysis. But it should be emphasized that qualification of the performance analysis evaluates its basic components in combination. That type of qualification does not separate the parts from the whole. In Chapters 6 and 7, it was possible to discuss the assumptions, approximations and limitations of the

models. That is not the case in the present chapter. The merits of the present end-wall boundary layer analysis cannot be established beyond demonstrating its effectiveness in supporting the methods of Chapters 6 and 7 to predict the overall performance of axial-flow compressors.

NOMENCLATURE

B = fractional area blockage
C = absolute velocity
c_f = skin friction coefficient
E = entrainment function
f = blade force
g = blade row staggered spacing
H = boundary layer streamwise shape factor
H_1 = boundary layer meridional shape factor
H_2 = boundary layer tangential shape factor
K_B = blockage factor
m = meridional coordinate and tangential velocity profile exponent
$\dot{m}$ = mass flow rate
n = meridional velocity profile exponent
P = pressure
q = inlet dynamic head
Re_θ = momentum thickness Reynolds number
r = radius
s = blade pitch
U_{leak} = leakage flow tangential velocity
V = velocity relative to the wall
W = velocity relative to the blade row
y = distance normal to the wall
β = flow angle
γ = blade stagger angle
Δ = leakage flow correction parameter
δ = boundary layer thickness
δ_c = blade clearance
δ^* = boundary layer streamwise displacement thickness
δ_1^* = boundary layer meridional displacement thickness
δ_2^* = boundary layer tangential displacement thickness
θ = tangential coordinate and streamwise momentum thickness
θ_{11} = meridional momentum thickness
θ_{12} = tangential momentum flux thickness
θ_{22} = tangential momentum thickness
μ = fluid viscosity
ν = blade force defect thickness
ρ = fluid density
τ = shear stress
ϕ = contour angle with the axial direction
ψ = pressure coefficient
ω = rotation speed

Subscripts

e = boundary layer edge condition
in = blade inlet condition
$leak$ = seal leakage parameter
m = meridional component
out = blade discharge condition
s = streamwise component
w = wall condition
θ = tangential component

Superscripts

$'$ = parameter in rotating coordinates
$\bar{}$ = average of blade inlet and discharge values
+ = upstream leakage flow correction
- = downstream leakage flow correction

8.1 HISTORICAL DEVELOPMENT OF END-WALL BOUNDARY LAYER THEORY

Early attempts to account for the effects of end-wall boundary layer blockage relied on assigned blockage factors. Typical practice was to assign the fractional area blockage to vary linearly through the compressor (e.g., Sandercock et al., 1954). Alternatively, the boundary layer displacement thickness or the blockage was assumed to vary linearly through the front stages and remain constant in the rear stages (e.g., Voit, 1953; Jansen and Moffet, 1967). These blockage allowances were rather arbitrary, based largely on the investigator's experience from previous compressors. Indeed, they really were rather arbitrary corrections that appeared to explain differences between calculated and measured compressor performance. Considering the relatively crude calculation methods used, these corrections probably compensated for many weaknesses and omissions in the analyses in addition to the end-wall boundary layer blockage effects.

Early attempts to compute end-wall boundary layer blockage in multistage compressors using boundary layer analysis techniques were published simultaneously by Stratford (1967) and Jansen (1967). Both methods seek to predict the average boundary layer growth assuming that the blade forces are conserved inside the boundary layer and that the stream surface slope can be neglected. This reduces the problem to consideration of a simplified axial momentum-integral equation similar to Eq. (3-52) but with $\sin\phi = v_m = 0$. These assumptions uncouple the axial momentum-integral equation from the tangential momentum-integral equation, so that Eq. (3-53) is unnecessary. Stratford employed flat-plate approximations for the boundary layer shape factor, H, and the wall shear stress. Jansen used an approximate integral solution (Schlicting, 1968 and 1979). Subsequent investigations showed that these early analyses are overly simplified. Nevertheless, they introduced the important concept of analyzing the gap-averaged or pitch-averaged boundary layer flow using integral boundary layer analysis techniques.

Smith (1970) reported detailed end-wall boundary layer data measured in a multistage axial-flow compressor. His measurements clearly demonstrate that blade forces are not constant across the boundary layer. He also provides experimental evidence to support the "repeating stage model." Basically this model assumes that the end-wall boundary layers achieve an equilibrium condition after passing through several stages, such that the blade row exit and inlet flow profiles are essentially identical. Once the equilibrium condition is reached, boundary layer growth is viewed as primarily a function of aerodynamic loading. Smith suggests that the repeating stage concept has been recognized for many years (e.g., Howell, 1947), but has not been used effectively. Smith provides experimental boundary layer data that may provide at least a preliminary basis for using this model. In a subsequent publication (Koch and Smith, 1976), the same basic boundary layer data was reworked as a sum of the hub-and-shroud boundary layers, as shown in Figs. 8-1 and 8-2. The combined data show less data scatter as compared to Smith (1970). The pressure coefficient, ψ, is a sum of the rotor and stator pressure coefficients for the stage, specifically defined by

$$\psi = \frac{\Delta p_{rotor} + \Delta p_{stator}}{q_{rotor} + q_{stator}} \tag{8-1}$$

where q is the inlet dynamic head. The meridional displacement thickness, δ_1^*, and the tangential force defect thickness, v_θ, are defined in Eqs. (3-54) and (3-60),

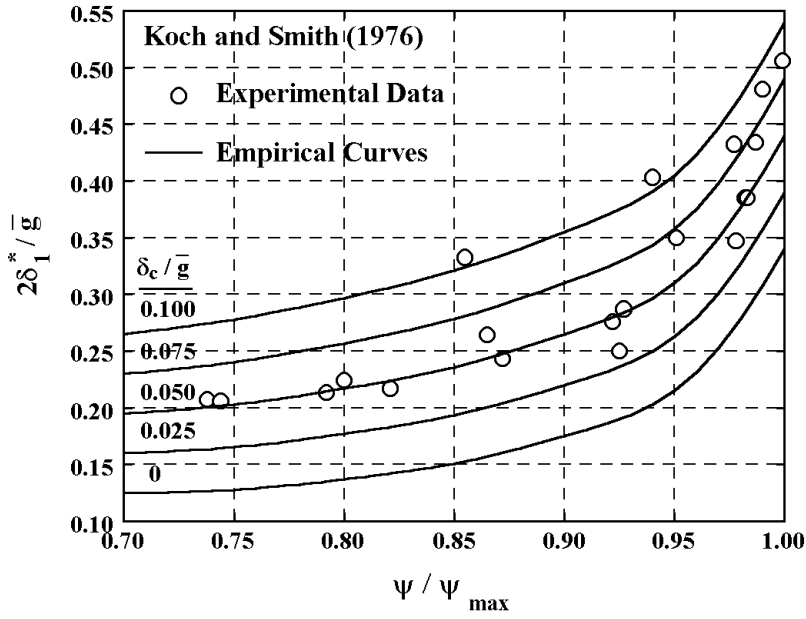

FIGURE 8-1 Displacement Thickness Data

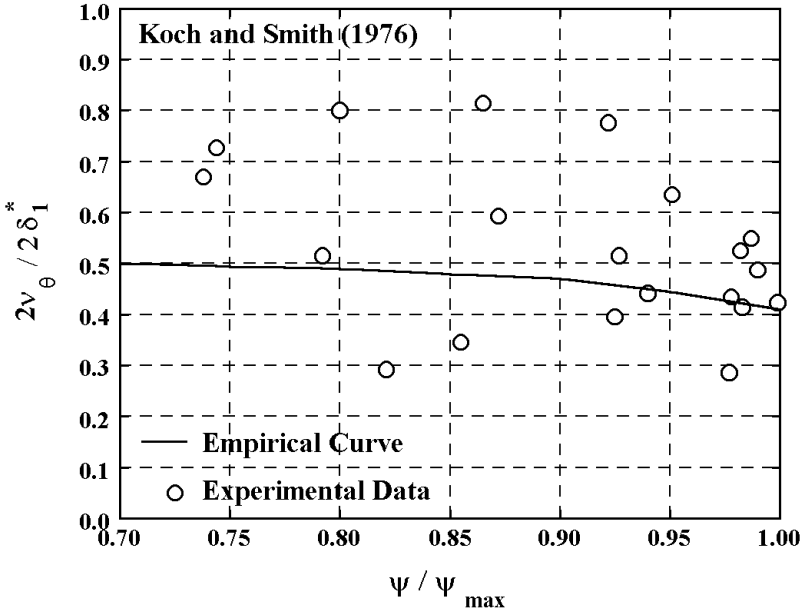

FIGURE 8-2 Tangential Force Defect Data

and δ_c is the blade tip clearance. The staggered spacing, g, is a function of the blade pitch, s, and stagger angle, γ, where average values are used,

$$\bar{g} = \bar{s} \cos \bar{\gamma} \tag{8-2}$$

Hunter and Cumpsty (1982) report similar results obtained with an isolated rotor. Koch and Smith use the empirical curves shown in Fig. 8-1 to estimate the sum of the displacement thicknesses or blockage. This requires that ψ_{max} values be supplied by some unspecified stall criterion. The displacement thicknesses plus the tangential force defect are then used to estimate the efficiency reduction due to end-wall losses. There is no doubt that Smith made a substantial contribution to our knowledge of end-wall boundary layers. But there is little reason to believe that the empirical models outlined can be used for general application. To recognize that the empirical curves shown are far from correlations of experimental results, one need only note that the tip clearance-to-staggered spacing ratios for all experimental data in Fig. 8-1 lie between 0.028 and 0.062. Careful study of the original reference shows that the experimental data trends contradict the empirical curves about as often as they are in agreement. And the excessive data scatter in Fig. 8-2 provides no real basis for any empirical correlation of the tangential force defect. Although far from a complete end-wall flow model, these references provide important insight into the end-wall boundary layer problem. It is clear that any end-wall boundary layer theory must address the

problem of blade force defects. Substantial tangential force defects clearly do exist. It must be presumed that the same is likely to be true for meridional force defects. But the repeating stage model poses special constraints. For an equilibrium blockage to be established, it is clear that meridional blade force defects must become small, or possibly even negative. Unfortunately, none of the above experimental investigations provided any direct insight relative to the meridional force defect behavior. It is apparent that our knowledge of the mechanisms behind the blade force defects is far from adequate to support an accurate end-wall loss calculation method.

There have been numerous attempts to formulate end-wall boundary layer analyses since the original attempts by Stratford and Jansen. One of most significant was the work of Mellor and Wood (1971), who provided a rather rigorous development of the basic gap-averaged governing equations. Their development includes effects previously neglected, such as blade force defects and "jump" conditions, to treat boundary layers moving between rotating and stationary frames of reference. They conducted numerous analytical studies to show how these phenomena can be used to explain observed flow behavior not modeled by the simpler methods. Like Smith (1970), Mellor and Wood considered the need to explain the existence of a repeating stage condition to be important. Balsa and Mellor (1975) continued this development by attempting to formulate a usable end-wall boundary layer analysis. In a serious attempt to address the blade force defect problem, the difference in the tangential and meridional momentum defect thicknesses was approximated with a secondary flow model. It was also assumed that the overall blade force remains approximately normal to the mean mainstream velocity vector. These conditions are sufficient to solve the governing equations and do offer a mechanism that can produce the repeating stage condition. This development includes techniques to convert boundary layer data into an end-wall loss prediction. Although undoubtedly the most complete theoretical development up to that time, several important features were largely ignored. The critically important boundary layer shape factor relating the displacement and momentum thicknesses was somewhat arbitrarily assigned to match predictions to experiment in sample overall compressor performance predictions. The boundary layer skin friction coefficient was treated in a similar fashion. The coupling between the tangential and meridional momentum-integral equations was ignored, even though it can be very significant when ϕ is not zero in Eqs. (3-52) and (3-53).

An important series of publications on this subject by Professor Hirsch and associates also should be mentioned. These include Hirsch (1974 and 1976) and De Ruyck et al. (1979 and 1980). These references provide a very detailed discussion of the important force defect terms and investigate various alternative blade force defect models derived from secondary flow theory. They also attempt to model some of the features that were handled rather arbitrarily by Balsa and Mellor. Although the results fall short of a complete end-wall boundary layer theory, these references provide considerable insight into the problem and are definitely recommended.

Basically, the current state of the art of end-wall boundary layer theory is insufficient to analyze the complete end-wall flow problem, including the associated end-wall losses. The prediction of end-wall boundary layer blockage to

support the aerodynamic performance analysis of axial-flow compressors is probably the best that can be expected. Nevertheless, the experimental and analytical studies discussed above have clearly identified several important features that strongly influence the end-wall flow problem. Even the more modest goal of predicting end-wall blockage effects requires consideration of the blade force defect terms and should include a mechanism that can produce the repeating stage condition.

8.2 THE END-WALL BOUNDARY LAYER EQUATIONS

End-wall boundary layer analysis in axial-flow compressors considers equations for the flow averaged over the pitch between adjacent blades. The governing equations are basically identical to the axisymmetric three-dimensional boundary layer equations presented in Chapter 3. Most investigators have ignored the streamline slope terms in the governing equations, basically assuming that $\phi = 0$. Also, it has been common practice to develop the governing equations in either stationary coordinates or in a coordinate system fixed to the blade rows. In the real problem, the wall and blades rotate at different speeds at the blade tips, unless an attached shroud is present. This effect is usually ignored, except perhaps as a correction to the wall shear stress. Aungier (2000) develops the end-wall boundary layer equations for use in centrifugal compressors, where these effects cannot be neglected. This more general form of the governing equations will be used here also. The absolute velocity will continue to be designated as C and the velocity relative to the blade by W. But the velocity relative to the wall is also needed, and will be designated by V. If the rotation speed of the blade is ω and the rotation speed of the wall is ω_w, the three velocities are related by

$$C_m = W_m = V_m \tag{8-3}$$

$$C_\theta = W_\theta + r\omega = V_\theta + r\omega_w \tag{8-4}$$

The no-slip condition requires that the fluid velocity at the wall must vanish in the coordinate system fixed to the wall. So the governing equations should be written in that coordinate system. The axisymmetric three-dimensional boundary layer equations presented in Chapter 3 are valid for any rotating coordinate system. So they are easily transformed to the coordinate system fixed to the wall by substituting V for W and ω_w for ω. Consequently, the governing equations for the end-wall boundary layer flow problem are easily shown to be

$$\frac{\partial}{\partial m}[r\rho_e V_{me}(\delta - \delta_1^*)] = r\rho_e V_e E \tag{8-5}$$

$$\begin{aligned}\frac{\partial}{\partial m}[r\rho_e V_{me}^2\theta_{11}] + \delta_1^* r\rho_e V_{me}\frac{\partial V_{me}}{\partial m} - \rho_e V_{\theta e}\sin\phi[V_{\theta e}(\delta_2^* + \theta_{22}) + 2\omega_w r\delta_2^*] \\ = r[\tau_{mw} + f_{me}v_m]\end{aligned} \tag{8-6}$$

$$\frac{\partial}{\partial m}[r^2\rho_e V_{me}V_{\theta e}\theta_{12}] + r\delta_1^*\rho_e V_{me}\left[r\frac{\partial V_{\theta e}}{\partial m} + \sin\phi(V_{\theta e} + 2r\omega_w)\right] = r^2[\tau_{\theta w} + f_{\theta e}v_\theta] \quad (8\text{-}7)$$

The blade forces at the boundary layer edge are

$$f_{me} = \rho_e V_{me}\frac{\partial V_{me}}{\partial m} + \frac{\partial P_e}{\partial m} - \frac{\sin\phi}{r}\rho_e(V_{\theta e} + \omega_w r)^2 \quad (8\text{-}8)$$

$$f_{\theta e} = \frac{\rho_e V_{me}}{r}\left[r\frac{\partial V_{\theta e}}{\partial m} + \sin\phi(V_{\theta e} + 2r\omega_w)\right] = \frac{\rho_e V_{me}}{r}\frac{\partial rC_{\theta e}}{\partial m} \quad (8\text{-}9)$$

Equations (8-7) and (8-9) can be combined to yield

$$\frac{\partial}{\partial m}[r^2\rho_e V_{me}V_{\theta e}\theta_{12}] + r^2\delta_1^* f_{\theta e} = r^2[\tau_{\theta w} + f_{\theta e}v_\theta] \quad (8\text{-}10)$$

If y is the distance normal to the wall and δ is the boundary layer thickness, the various defect thicknesses in the boundary layer equations are defined as

$$\rho_e V_{me}\delta_1^* = \int_0^\delta (\rho_e V_{me} - \rho V_m)dy \quad (8\text{-}11)$$

$$\rho_e V_{me}^2\theta_{11} = \int_0^\delta \rho V_m(V_{me} - V_m)dy \quad (8\text{-}12)$$

$$\rho_e V_{me}V_{\theta e}\theta_{12} = \int_0^\delta \rho V_m(V_{\theta e} - V_\theta)dy \quad (8\text{-}13)$$

$$\rho_e V_{\theta e}\delta_2^* = \int_0^\delta (\rho_e V_{\theta e} - \rho V_\theta)dy \quad (8\text{-}14)$$

$$\rho_e V_{\theta e}^2\theta_{22} = \int_0^\delta \rho V_\theta(V_{\theta e} - V_\theta)dy \quad (8\text{-}15)$$

$$v_m f_{me} = \int_0^\delta (f_{me} - f_m)dy \quad (8\text{-}16)$$

$$v_\theta f_{\theta e} = \int_0^\delta (f_{\theta e} - f_\theta)dy \quad (8\text{-}17)$$

Solution of this set of equations requires empirical correlations for the entrainment function, E, the wall shear stresses, τ_{wm} and $\tau_{w\theta}$, and the force defect thicknesses, v_m and v_θ. It also requires empirical relationships between the mass and momentum defect thicknesses, typically derived from some assumed form of the boundary layer velocity profiles.

8.3 THE BOUNDARY LAYER VELOCITY PROFILE ASSUMPTIONS

Aungier [1988(b)] obtained good agreement with experimental data for axisymmetric swirling flow in vaneless annular passages by solving the axisymmetric three-dimensional boundary layer equations using simple power-law velocity profile assumptions.

$$\frac{V_m}{V_{me}} = \left(\frac{y}{\delta}\right)^n \tag{8-18}$$

$$\frac{V_\theta}{V_{\theta e}} = \left(\frac{y}{\delta}\right)^m \tag{8-19}$$

Substitution of these profile assumptions into the definitions of the various mass and momentum defect thicknesses, assuming density can be regarded as essentially constant, yields the following relationships.

$$n = \theta_{11} / (\delta - \delta_1^* - 2\theta_{11}) \tag{8-20}$$

$$m = \theta_{12}(n+1)^2 / [\delta - \theta_{12}(n+1)] \tag{8-21}$$

$$H_1 = \delta_1^* / \theta_{11} = 2n + 1 \tag{8-22}$$

$$\delta - \delta_1^* = 2H_1\theta_{11} / (H_1 - 1) \tag{8-23}$$

$$\delta_1^* / \delta = n / (n+1) \tag{8-24}$$

$$H_2 = \delta_2^* / \theta_{22} = 2m + 1 \tag{8-25}$$

$$\delta_2^* / \delta = m / (m+1) \tag{8-26}$$

These profile assumptions and empirical relations require some modification when applied to flows through blade rows. This can be illustrated by considering the flow through an axial-flow compressor stage on the hub contour. For the rotor, the blades and the hub end-wall rotate at the same speed, so $V = W$ in the boundary layer equations. If the downstream stator is shrouded, both the hub end-wall and the blades are stationary, so $V = C$. From Eqs. (8-4) and (8-13), it is easily shown that the jump condition between the rotor exit and the stator inlet is

$$C_{\theta e}\theta_{12} = W_{\theta e}\theta'_{12} \tag{8-27}$$

The prime designates the tangential momentum defect thickness viewed in the rotating coordinate system. Since W_θ and C_θ normally have opposite signs, it can be seen that the tangential momentum defect thickness will change sign at any meridional station where the wall rotation speed changes from rotating to stationary, or inversely. Hence, the boundary layer velocity profile assumption must include cases where the θ_{12}, θ_{22} and δ_2^* are negative and $H_2 < 1$. In this simple

illustration, a deficit in tangential momentum in the rotating coordinate system corresponds to excess tangential momentum in the stationary coordinate system. The boundary layer equations can accommodate this jump condition, but the power-law profile assumption of Eq. (8-19) cannot. Aungier (2000) extended the power-law profile model to accommodate this situation. When $m < 0.05$, Eq. (8-19) is replaced by

$$\frac{V_\theta}{V_{\theta e}} = \left(\frac{y}{\delta}\right)^{0.05} + 0.1705(1-20m)\left(1-\frac{y}{\delta}\right)^2\left(\frac{y}{\delta}\right)^{0.1} \tag{8-28}$$

Figure 8-3 shows typical velocity profiles from Eqs. (8-19) and (8-28). Both equations yield identical results at $m = 0.05$. Equation (8-28) simply extends the power-law profiles in a plausible fashion to accommodate cases where the integrated tangential momentum in the boundary layer exceeds the boundary layer edge value, i.e., where m becomes negative. From Eqs. (8-18) and (8-28) and the various boundary layer defect thickness definitions,

$$\frac{\delta_2^*}{\delta} = \frac{20m}{21} \tag{8-29}$$

$$\frac{\theta_{22}}{\delta} = 0.95m - 1.684m^2 \tag{8-30}$$

$$m = 0.05 + \left[\frac{\theta_{12}}{\delta} - \frac{0.05}{(n+1)(n+1.05)}\right]\frac{(n+1.1)(n+2.1)(n+3.1)}{6.82} \tag{8-31}$$

$$H_2 = \frac{\delta_2^*}{\theta_{22}} = \frac{20}{21(0.95-1.684m)} \tag{8-32}$$

Figure 8-4 presents the functional relationship between m and H_2 from Eqs. (8-25) and (8-32).

If the entrainment equation is solved for $(\delta - \delta_1^*)$ and the momentum integral equations are solved for θ_{11} and θ_{12}, n and m can be computed from Eqs. (8-20) and (8-21) or (8-31). Then the boundary layer profile assumptions provide all other boundary layer data. This writer's analysis limits H_1 and H_2 to a maximum of 2.4, which is used as the boundary layer profile separation limit. Empirical models to compute the entrainment function, wall shear stresses and blade force defect thicknesses are required to complete the formulation of the analysis.

8.4 EMPIRICAL MODELS FOR ENTRAINMENT AND WALL SHEAR STRESS

The wall shear stress terms can be approximated using a suitable skin friction coefficient model. Assume that the shear stress is directed along the boundary layer edge streamline. Then the shear stress components are related to the skin friction coefficient, c_f.

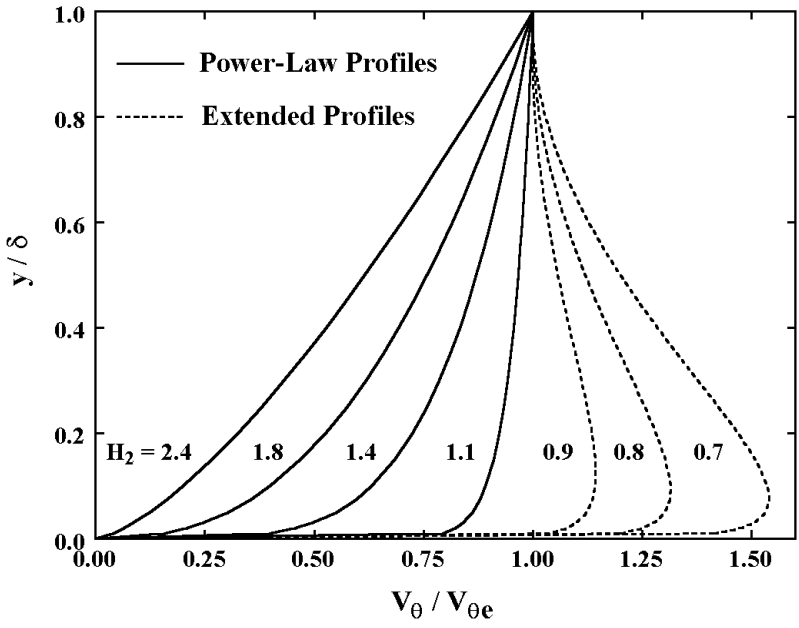

FIGURE 8-3 Extended Boundary Velocity Profiles

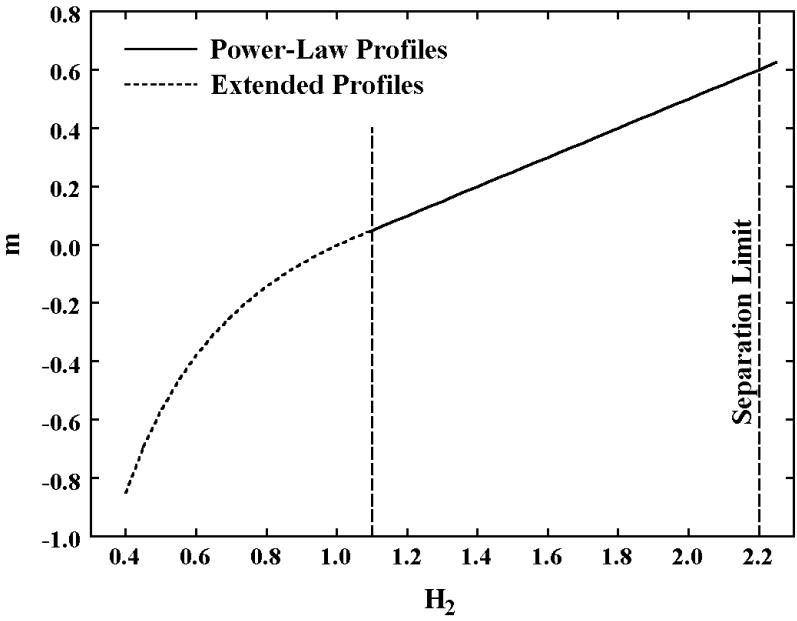

FIGURE 8-4 The Boundary Layer Shape Factor

$$c_f = \frac{\tau_w}{\frac{1}{2}\rho_e V_e^2} \tag{8-33}$$

$$\tau_{mw} = \tfrac{1}{2} c_f \rho_e V_e V_{me} \tag{8-34}$$

$$\tau_{\theta w} = \tfrac{1}{2} c_f \rho_e V_e V_{\theta e} \tag{8-35}$$

The well-known skin friction coefficient model by Ludwieg and Tillmann (1950) is one of the most accurate methods available for turbulent boundary layers. It can be expressed as

$$c_f = 0.246 \exp(-1.561H)(\rho_e V_e \theta / \mu)^{-0.268} \tag{8-36}$$

where θ and H are the momentum thickness and shape factor in the free stream direction, and μ is the fluid viscosity. Designate the free stream component of the fluid velocity within the boundary layer by V_s.

$$V_s = V_m \cos\beta_e + V_\theta \sin\beta_e \tag{8-37}$$

Noting that $V_{se} = V_e$, the defect thicknesses in the free stream direction are given by

$$\rho_e V_e^2 \theta = \int_0^\delta \rho V_s (V_e - V_s) dy \tag{8-38}$$

$$\rho_e V_e \delta^* = \int_0^\delta (\rho_e V_e - \rho V_s) dy \tag{8-39}$$

and $H = \delta^* / \theta$. Substituting Eq. (8-37) into Eqs. (8-38) and (8-39) yields expressions for these defect thicknesses in terms of the axisymmetric three-dimensional boundary layer defect thicknesses.

$$\delta^* = \delta_1^* \cos^2\beta_e + \delta_2^* \sin^2\beta_e \tag{8-40}$$

$$\theta = (\theta_{11} + \delta_1^*)\cos^4\beta_e + (\theta_{22} + \delta_2^*)\sin^4\beta_e + 2(\theta_{12} + \delta_1^*)\sin^2\beta_e \cos^2\beta_e - \delta^* \tag{8-41}$$

Some care is required to avoid values of these defect thicknesses that will invalidate Eq. (8-36). It is recommended that all defect thicknesses on the right-hand side of Eqs. (8-40) and (8-41) be limited to be no less than zero. In addition, when solving Eq. (8-36), it is recommended that $H \le 2.4$ be required, where $H = 2.4$ is regarded as a boundary layer separation limit. The momentum thickness Reynolds number in Eq. (8-36) should be limited to a value to ensure that transition to turbulent flow has occurred. A reasonable transition limit for this purpose is to require $\rho_e V_e \theta / \mu \ge 250$.

When solving the boundary layer equations in blade free passages, this writer has observed that the entrainment function is best approximated by

$$E = 0.025(H_1 - 1) \tag{8-42}$$

Since gradients in the tangential direction all vanish for these cases, it is not too surprising that the shape of the meridional flow profile controls the fluid entrainment at the boundary layer edge. This approach was adopted by Davis (1976) at this writer's suggestion and has also been shown to be effective by Aungier [1988(b)] and Schumann (1985). When solving the boundary layer equations within a blade passage, where the flow is guided by the blades, the free stream shape factor, H, is more relevant, much like the case in classical two-dimensional boundary layer theory, i.e.,

$$E = 0.025(H - 1) \tag{8-43}$$

For the present application to axial-flow compressor performance analysis, the boundary layer equations are normally solved across blade rows. Equation (8-43) is also used in this case, even though the solution is carried out using data outside the blade passage, where the flow is considered to be axisymmetric. In this case, the boundary layer development occurs primarily within the blade passage where the flow is guided by the blades. Hence the entrainment process should be governed in the same way as when solving within a blade passage.

8.5 THE BLADE FORCE DEFECT THICKNESSES

The important blade force defect thicknesses need to be specified. The best available experimental data is the tangential blade force defect data by Koch and Smith (1976) shown in Fig. 8-2, along with an empirical curve used by them. Koch and Smith used the empirical curve to estimate end-wall losses. They proposed a separate correlation for end-wall blockage as illustrated in Fig. 8-1. It is evident that the empirical curve in Fig. 8-2 does not correlate to the experimental data with sufficient accuracy for it to be used in predicting end-wall blockage. This writer has reworked the data of Koch and Smith in the form shown in Fig. 8-5. Staggered spacing is used to normalize ν_θ instead of the displacement thickness. Since ν_θ is known to increase with blade clearance (Hunter and Cumpsty, 1982), it was somewhat arbitrarily corrected by subtracting half of the average blade clearance. Data scatter remains significant, but the result does appear to suggest trends that might be used in an empirical correlation, such as the empirical curve shown in Fig. 8-5. In the rare cases where the boundary layer thickness is less than the blade clearance, this model yields very questionable results. It is unlikely that ν_θ can become significant until the flow about the blade profiles comes under the influence of the distorted boundary layer flow profiles. To avoid that weakness, the data from Fig. 8-5 was expressed in the form shown in Fig. 8-6, which seems equally satisfactory as the basis for an empirical correlation.

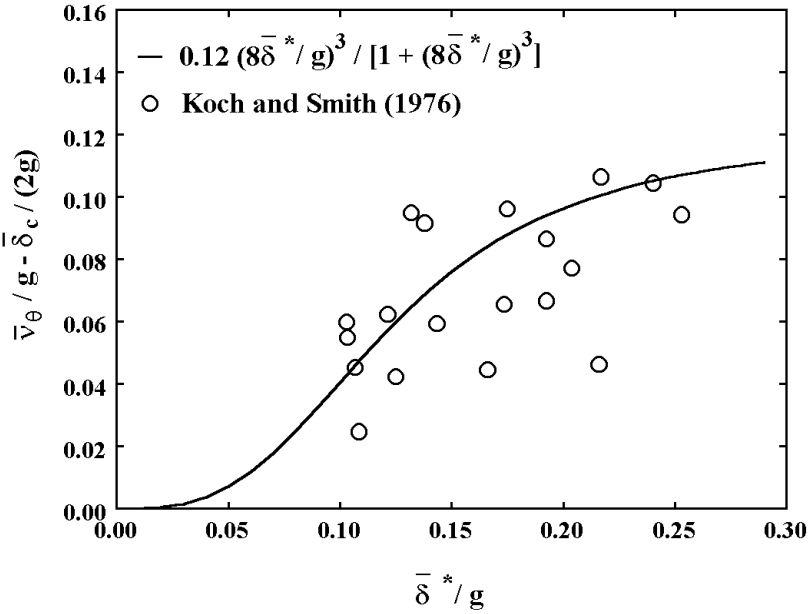

FIGURE 8-5 Tangential Force Defect Model

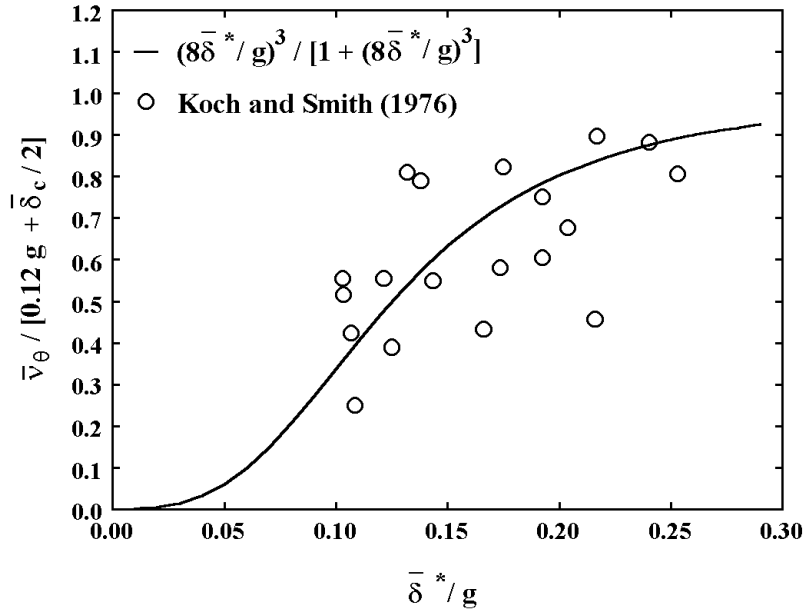

FIGURE 8-6 Adjusted Tangential Force Defect Model

For the purpose of end-wall blockage prediction, the more critical parameter is the meridional blade force defect thickness, v_m. There are diverse and contradictory opinions concerning v_m and no experimental data available for guidance. Smith (1970) and Koch and Smith (1976) argue that v_m must be small based on the existence of the repeating stage condition. Balsa and Mellor (1975) argue that the blade force should remain approximately normal to the free streamline, similar to the blade force components at the boundary layer edge. This assumes that $v_m = v_\theta$, since both are governed by the same fundamental fluid dynamics. They also consider the need to explain the repeating stage condition to be a basic requirement. They assume that the blades guide the flow toward a collateral flow condition such that θ_{11} and θ_{12} approach a common value at the blade discharge, but with a correction for blade clearance effects. In this way, small or even negative values of v_m are possible to provide the mechanism for the repeating stage condition. De Ruyck and Hirsch (1980) propose a correlation for v_m with secondary flow parameters, but impose a transverse force defect correction similar to that of Balsa and Mellor. None of these models has been found to be particularly effective for end-wall blockage prediction, although the model of Balsa and Mellor provided the most promising results. Hence, this writer's blade force defect model is an adaptation of that method.

Following Balsa and Mellor (1975) it is assumed that the blade force remains oriented in the same direction as the free stream blade force such that $v_m = v_\theta$. Hence the subscript can be omitted and the blade force defect simply designated as v. A base defect thickness is estimated as

$$v_0 = \frac{(0.12g + \delta_c / 2)(8\bar{\theta}_{11} / g)^3}{1 + (8\bar{\theta}_{11} / g)^3} \tag{8-44}$$

This equation is similar to the empirical curve shown in Fig. 8-6. The average meridional momentum thickness is used instead of the displacement thickness because it is less likely to be subject to abrupt changes during the analysis. It had been expected that the equation would require adjustment by some multiplying factor to compensate for the change in the independent variable relative to the correlation in Fig. 8-6. It was somewhat of a surprise to find that qualification of the performance analysis against experimental performance indicated that no adjustment is necessary. Indeed, for most of the axial-flow compressors analyzed in the qualification study, Eq. (8-44) was quite sufficient to provide very good performance prediction accuracy using the models presented in this Chapter and in chapters 6 and 7. But a few cases were encountered where the blade force defects from Eq. (8-44) appeared to overestimate the blockage. Based on the previous discussions, this is to be expected. It is clear that the blade force defect must become small or even negative if the flow in the compressor approaches the repeating stage condition. A correction procedure not unlike that of Balsa and Mellor was found effective in correcting the blade force defect from Eq. (8-44) in those cases. If the blades provide sufficient guidance to the flow to force the boundary layer to be completely collateral at the discharge, θ_{11} and θ_{12} will approach a common value when viewed in a coordinate system fixed to the blades. Regarding W as the velocity relative to the blade row being considered, this requires that the boundary layer at the blade discharge satisfy the following condition:

$$V_\theta \theta_{12} - W_\theta \theta_{11} = 0 \tag{8-45}$$

As noted in Eq. (8-27), the first term in Eq. (8-45) is identical to the tangential momentum defect in the coordinate system fixed to the blade row. If we use a prime to designate the tangential momentum thickness in the coordinate system fixed to the blade row, Eq. (8-45) can be written as

$$W_\theta \theta'_{12} - W_\theta \theta_{11} = 0 \tag{8-46}$$

Hence Eq. (8-45) is the condition for collateral flow. If Eq. (8-10) is integrated across the blade row of interest, the meridional momentum thickness at the discharge can be represented by

$$V_{\theta e} \theta_{12} = A + \nu \frac{\bar{r}^2 f_{\theta e} \Delta m}{r^2 \rho_e V_{me}} \tag{8-47}$$

Similarly, integrating Eq. (8-6) across the blade row and multiplying by $W_{\theta e}$ yields

$$W_{\theta e} \theta_{11} = B + \nu W_{\theta e} \frac{\bar{r} f_{me} \Delta m}{r \rho_e V_{me}^2} \tag{8-48}$$

For convenience, assume that the blade force is normal to the mean free stream velocity, i.e.,

$$f_{me} = -\overline{W}_{\theta e} f_{\theta e} / \overline{V}_{me} \tag{8-49}$$

$$W_{\theta e} \theta_{11} = B - \nu W_{\theta e} \frac{\bar{r} f_{\theta e} \Delta m}{r \rho_e V_{me}^2} \frac{\overline{W}_{\theta e}}{\overline{V}_{me}} \tag{8-50}$$

If a blade force defect increment $\Delta\nu$ is imposed, Eqs. (8-47) and (8-50) yield

$$\Delta(V_{\theta e} \theta_{12} - W_{\theta e} \theta_{11}) = \Delta\nu \left[\frac{\bar{r}}{r} + \frac{\overline{W}_{\theta e} W_{\theta e}}{\overline{V}_{me} V_{me}} \right] \frac{\bar{r} f_{\theta e} \Delta m}{r \rho_e V_{me}} \tag{8-51}$$

This can be used to calculate the increment in the blade force defect thickness needed to impose the collateral flow condition, i.e.,

$$\Delta(V_{\theta e} \theta_{12} - W_{\theta e} \theta_{11}) = \xi \Delta\nu = -(V_{\theta e} \theta_{12} - W_{\theta e} \theta_{11}) \tag{8-52}$$

where

$$\xi = \left[\frac{\bar{r}}{r} + \frac{\overline{W}_{\theta e} W_{\theta e}}{\overline{V}_{me} V_{me}} \right] \frac{\bar{r} f_{\theta e} \Delta m}{r \rho_e V_{me}} \tag{8-53}$$

In practice, the solidity would have to be infinite for the blade guidance to be sufficient to force collateral flow in the boundary layer. Hence the condition imposed in the analysis is

$$\Delta v = -(V_{\theta e}\theta_{12} - W_{\theta e}\theta_{11})F / \xi \tag{8-54}$$

Since a correction appeared to be required only in cases where the blockage and defect force thicknesses become relatively large, it was reasonable to expect F to be similar in form to the correlation for v_0, which proved to be true.

$$F = \frac{1}{2}\frac{(8\bar{\theta}_{11}/g)^3}{1+(8\bar{\theta}_{11}/g)^3} \tag{8-55}$$

Note that F is similar in form to the function illustrated in Fig. 8-5, but approaches one-half as the quantity $(8\theta_{11}/g)$ becomes large. The overall blade force defect thickness is given by

$$v = v_0 + \Delta v \tag{8-56}$$

Equation (8-54) is to be solved using boundary layer data obtained with $\Delta v = 0$. In practice, it is preferable to correct the blade force defect thickness continually as the governing equations are being solved in an iterative fashion. That can be done as long as the correction process accounts for any non-zero value of Δv used in the previous iteration. It can easily be shown that updates for Δv on all iterations can be imposed as

$$\Delta v \rightarrow [\Delta v - (V_{\theta e}\theta_{12} - W_{\theta e}\theta_{11})/\xi]F \tag{8-57}$$

8.6 SEAL LEAKAGE EFFECTS FOR SHROUDED BLADES

When the blade row is shrouded at the end-wall being analyzed, the boundary layer data must be corrected for the shroud seal leakage. The shroud seal leakage mass flow calculation has been described in Chapter 6. The sign convention used for the leakage mass flow is positive when the leakage is directed from the blade row discharge to the inlet, as illustrated in Fig. 8-7. The shroud seal leakage will change the mass flow rate in the boundary layer. The leakage flow is expected to have no meridional velocity component, so the boundary layer meridional momentum flow rate should be unchanged. The absolute tangential velocity of the leakage flow entering the boundary layer is assumed to be half of the local speed of the rotating wall. If the leakage flow is out of the boundary layer, its tangential velocity relative to the wall is assumed to be essentially zero, due to the no-slip condition. The details of the mass and momentum balances to account for the leakage flow will be left to the exercises. Here, only the results will be given. Using the nomenclature defined in Fig. 8-7, the blade row inlet boundary layer mass flow is corrected by

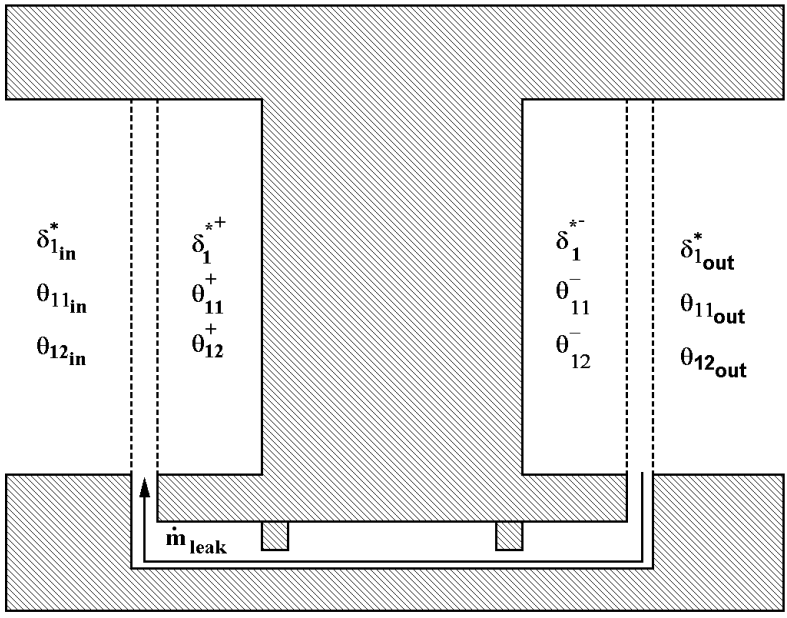

FIGURE 8-7 A Shrouded Blade Row

$$(\delta - \delta_1^*)^+ = (\delta - \delta_1^*)_{in} + \Delta^+ \tag{8-58}$$

$$\Delta^+ = \frac{\dot{m}_{leak}}{(2\pi r \rho_e V_{me})_{in}} \tag{8-59}$$

The meridional momentum balance yields

$$\theta_{11}^+ = \theta_{11_{in}} + \Delta^+ \tag{8-60}$$

If ω_c is the compressor rotation speed, the tangential velocity of leakage flow entering the boundary layer, relative to the blade shroud, is

$$U_{leak} = \tfrac{1}{2} r\omega_c + V_\theta - C_\theta \tag{8-61}$$

The tangential momentum balance, for either positive or negative leakage mass flow rate, yields

$$(V_\theta \theta_{12})^+ = (V_\theta \theta_{12})_{in} + \Delta^+ V_{\theta_{in}} - \tfrac{1}{2}(\Delta^+ + |\Delta^+|) U_{leak} \tag{8-62}$$

These leakage corrected boundary layer data are sufficient to define the power-law profile and correct all other boundary layer parameters using Eqs. (8-20) through (8-26). The boundary layer analysis is conducted across the blade row, with the wall rotation speed set equal to the blade rotation speed. Then mass and momentum balances and Eqs. (8-20) through (8-26) are used to correct the calculated discharge boundary layer data for the seal leakage to obtain the final blade discharge boundary layer data.

$$\Delta^- = \frac{\dot{m}_{leak}}{(2\pi r \rho_e V_{me})_{out}} \tag{8-63}$$

$$(\delta - \delta_1^*)_{out} = (\delta - \delta_1^*)^- - \Delta^- \tag{8-64}$$

$$\theta_{11_{out}} = \theta_{11}^- - \Delta^- \tag{8-65}$$

$$(V_\theta \theta_{12})_{out} = (V_\theta \theta_{12})^- - \Delta^- V_{\theta_{out}} + \tfrac{1}{2}(\Delta^- - |\Delta^-|)U_{leak} \tag{8-66}$$

8.7 BOUNDARY LAYER JUMP CONDITIONS

The boundary layer analysis has been developed in terms of the fluid velocity relative to the wall, where the wall may be stationary or rotating. It is necessary to consider jump conditions for cases where the boundary layer moves from a stationary wall to a rotating wall, or inversely. Indeed, the boundary layers along the hub contour in axial-flow compressors with shrouded stator blades must make this transition at every blade row. For clarity, designate the velocity relative to the wall rotating at rotation speed ω as W and C to be the velocity relative to the stationary wall. Boundary layer parameters relative to the rotating wall will be designated with a prime. Hence,

$$W_\theta = C_\theta - \omega r \tag{8-67}$$

Substituting Eq. (8-67) into the definitions of the various boundary layer defect thicknesses yields

$$C_{\theta_e}\theta_{12} = W_{\theta_e}\theta'_{12} \tag{8-68}$$

$$C_{\theta_e}\delta_2^* = W_{\theta_e}\delta_2'^* \tag{8-69}$$

$$C_{\theta_e}^2\theta_{22} = W_{\theta_e}^2\theta'_{22} + \omega r W_{\theta_e}\delta_2'^* \tag{8-70}$$

$$C_{\theta_e}^2\theta_{22}(1+H_2) = W_{\theta_e}^2\theta'_{22}(1+H'_2) + 2\omega r W_{\theta_e}\delta_2'^* \tag{8-71}$$

Equations (8-68) and (8-71) contain basic terms in the momentum-integral equations. Note that they have identical values in either rotating or stationary coordinates, so no special logic is required to convert them at a transition between a rotating and stationary wall. Consequently, integration of the governing

equations can proceed through the compressor without any complex logic at transitions between rotating and stationary walls.

8.8 SOLUTION PROCEDURE

Since the end-wall boundary layer analysis presented in this chapter considers only turbulent boundary layers, boundary layer data must be specified at the compressor inlet. The data needed are θ_{11}, θ_{12}, H_1 and H_2. It is reasonable to start the analysis with $H_1 = 1.4$, which is a typical value for simple flat-plate boundary layer flow. The classical one-seventh power-law profile is a reasonable choice for the tangential velocity profile, i.e., $m = 1 / 7$ or $H_2 = 1.286$. The boundary layer fractional area blockage, B, is assigned at the inlet. Assume the blockage is equally split between the hub-and-shroud contours and compute the meridional displacement thickness for either end-wall by

$$2\pi r \rho_e V_{me} \delta_1^* = \frac{1}{2} B \dot{m} \tag{8-72}$$

Equations (8-22) through (8-26) provide all other initial boundary layer data. If the analysis is to be started immediately upstream of the first blade row, experience has shown that $B = 0.02$ is a good choice. If the analysis can be started well upstream of the first blade row, a very small value can be entered for B so that the boundary layer development ahead of the first blade row is predicted by the analysis. Throughout the analysis, the boundary layer is always constrained to be turbulent by imposing a limit on the Reynolds number based on θ_{11}, i.e.,

$$\mathrm{Re}_\theta = \rho_e V_e \theta_{11} / \mu \geq 250 \tag{8-73}$$

Hence, specifying a very small value of B at the inlet station forces the analysis to start with a boundary layer essentially at the transition point from laminar to turbulent flow.

The analysis on each end-wall can be accomplished with a simple marching technique, starting at the second meridional station, and completing the solution at each station before proceeding to the next. The basic procedure is

1. Impose the inlet shroud seal leakage corrections of Section 8.6, if applicable. Estimate initial values of the momentum thicknesses from the upstream station using simplified forms of Eqs. (8-6) and (8-7).

$$\frac{\partial}{\partial m}[r \rho_e V_{me}^2 \theta_{11}] = 0 \tag{8-74}$$

$$\frac{\partial}{\partial m}[r^2 \rho_e V_{me} V_{\theta e} \theta_{12}] = 0 \tag{8-75}$$

   Assume H_1 and H_2 are equal to the upstream values and initialize all other parameters using Eqs. (8-22) through (8-26).

2. Compute the entrainment function and the wall shear stresses as described in Section 8.4. If applicable, compute the blade force defect using the methods described in Section 8.5.
3. Integrate Eq. (8-5) for $(\delta - \delta_1^*)$, Eq. (8-6) for θ_{11}, and Eq. (8-7) for θ_{12}.
4. Compute n and δ from Eqs. (8-20) and (8-24). As a precaution, require $\theta_{12} \le 0.99\delta/(n+1)$. Compute m from Eq. (8-21).
5. Compute the other boundary layer parameters from Eqs. (8-22) through (8-26).
6. Check for convergence on θ_{11}, H_1 and v. If not converged, return to Step 2 and repeat.
7. Impose the discharge shroud seal leakage corrections of Section 8.6, if applicable.
8. Return to Step 1 and treat the next meridional station until all stations have been analyzed.

When the boundary layer analysis is completed at all meridional stations on both end-walls, the end-wall boundary layer blockage and the blockage factor can be computed at all meridional stations for use in the meridional through-flow analysis of Chapter 7. If $\dot{m}$ is the compressor mass flow rate, they are given by

$$B = \sum_{Hub}^{Shroud} 2\pi r \rho_e V_{me} \delta_1^* / \dot{m} \tag{8-76}$$

$$K_B = 1 - B \tag{8-77}$$

Since the boundary layer and through-flow analyses are conducted sequentially in an iterative fashion, some limits and numerical damping are normally required. The boundary layer edge parameters may be quite unrealistic in the early iterations, resulting in rapid changes in the predicted blockage values.

8.9 TYPICAL RESULTS

Figures 8-8 through 8-10 illustrate end-wall blockage predictions from this end-wall boundary layer analysis for three different styles of axial-flow compressors. The NACA 8-stage compressor (Voit, 1953) is designed with two inlet transonic stages. The NACA 10-stage compressor (Johnsen, 1952) is a conservative design using all subsonic stages. The NACA 5-Stage compressor (Kovach and Sandercock, 1961) is designed with all transonic stages. The analysis of the NACA 10-stage compressor had to be started at the exit of an undefined inlet guide vane using measured vane discharge flow angles. The inlet blockage is set to 2% of the annulus area as recommended above. The analyses of the other two compressors started well up in the inlet passage with minimum (transition point) blockage levels to let the boundary layer develop naturally based on the analysis. It is seen that blockage levels and blockage distributions predicted for these three compressors are quite different, and show considerable variation of blockage level with overall pressure ratio, P_R. It will be seen in Chapter 9 that the overall

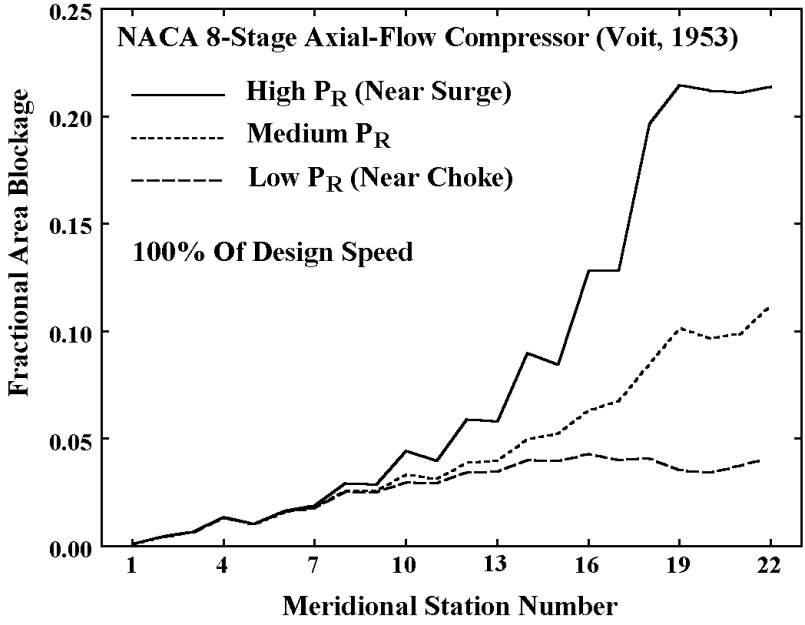

FIGURE 8-8 NACA 8-Stage Compressor Blockage

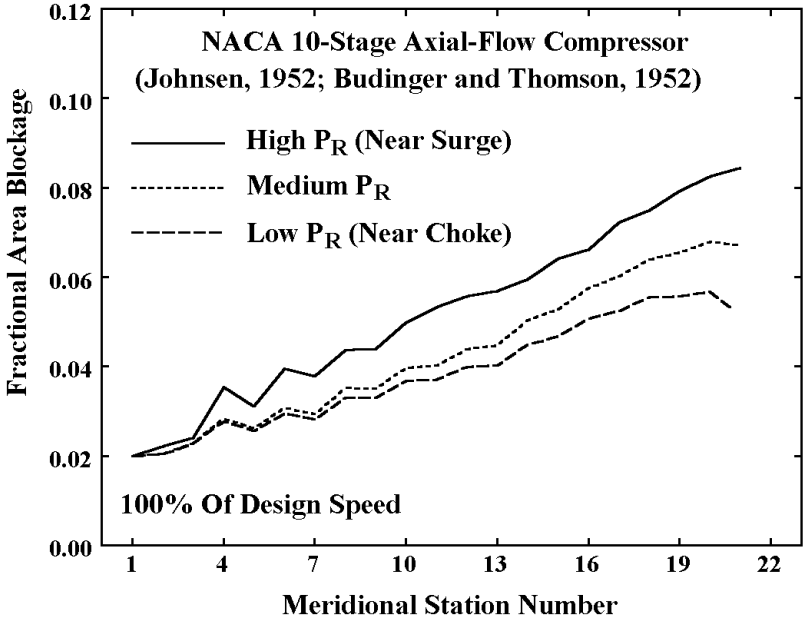

FIGURE 8-9 NACA 10-Stage Compressor Blockage

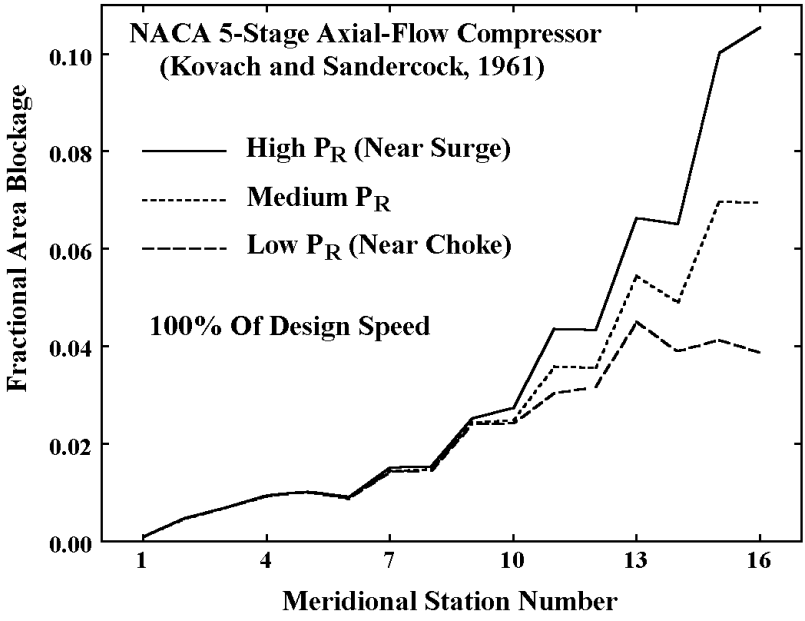

FIGURE 8-10 NACA 5-Stage Compressor Blockage

performance predictions obtained using these end-wall boundary layer blockage predictions are quite accurate for all of these compressors. Hence, the present end-wall boundary layer analysis is quite effective in its intended role of supporting the aerodynamic performance analysis.

EXERCISES

8.1 Consider the inlet of the shrouded stator blade shown in Fig. 8-7. From conservation of mass for the upstream boundary layer and the leakage mass flow, derive Eq. (8-58) for the boundary layer downstream of the injected leakage flow. The velocity, V, is relative to the blade shroud,

8.2 The leakage mass flow in Exercise 8.1 enters with $V_m = 0$. From conservation of meridional momentum for the upstream boundary layer and the leakage mass flow, derive Eq. (8-60) for the boundary layer downstream of the injected leakage flow.

8.3 The leakage mass flow in Exercise 8.1 enters with tangential velocity $U_{leak,}$ relative to the blade shroud. From conservation of tangential momentum for the upstream boundary layer and the leakage mass flow, derive Eq. (8-62) for the boundary layer downstream of the injected leakage flow.

8.4 Repeat Exercises 8.1 through 8.3 for the discharge of the stator blade, noting that the tangential velocity of the leakage flow leaving the boundary layer, relative to the blade shroud, is zero.

8.5 $(\delta - \delta_1^*)$, θ_{11} and θ_{12} are the boundary layer parameters obtained from the basic conservation equations. Develop expressions for these parameters as functions of n, m and δ, using Eqs. (8-11), (8-12), (8-13), (8-18) and (8-19). Use the results to derive Eqs. (8-20) and (8-21).